Scalable and reusable micro-bubble removal method to flatten large-area 2D materials

Phi H. Q. Pham, Nhi V. Quach, Jinfeng Li, and Peter J. Burke

Citation: Appl. Phys. Lett. **112**, 163106 (2018); doi: 10.1063/1.5022057
View online: https://doi.org/10.1063/1.5022057
View Table of Contents: http://aip.scitation.org/toc/apl/112/16
Published by the American Institute of Physics

Scalable and reusable micro-bubble removal method to flatten large-area 2D materials

Phi H. Q. Pham, Nhi V. Quach, Jinfeng Li, and Peter J. Burke[a)]
Department of Electrical Engineering and Computer Science, University of California, Irvine, California 92697, USA

(Received 10 January 2018; accepted 10 April 2018; published online 20 April 2018)

Bubbles generated during electro-delamination and chemical etch during large-area two-dimensional (2D) material transfer has been shown to cause rippling, and consequently, results in tears and wrinkles in the transferred film. Here, we demonstrate a scalable and reusable method to remove surface adhered micro-bubbles by using hydrophobic surfaces modified by self-assembled monolayers (SAMs). Bubble removal allows the 2D film to flatten out and prevents the formation of defects. Electrical characterization was used to verify improved transfer quality and was confirmed by increased field-effect mobility and decreased sheet resistance. Raman spectroscopy was also used to validate enhanced electrical quality following transfer. The bubble removal method can be applied to an assortment of 2D materials using diverse hydrophobic SAM variants. Our studies can be integrated into large scale applications and will lead to improved large-area 2D electronics in general. *Published by AIP Publishing*. https://doi.org/10.1063/1.5022057

Chemical vapor deposition (CVD) has enabled the synthesis of large-area two-dimensional (2D) materials including graphene,[1–3] transition metal dichalcogenides,[4,5] and hexagonal boron nitride.[6] In order to fabricate practical devices, the synthesized materials often require various wet-transfer processes which rely on removing the CVD-grown material from the growth substrate,[7,8] usually by chemical etching[9] or electro-delamination.[10,11] During these steps, the formation of bubbles between the 2D material and etch/delamination solution lead to rippling and detrimental defects,[7,12] and hence, developed processes have specifically aimed to minimize bubble formation by using low concentration of etchant[13] or low voltages during delamination.[10,14] Although the formation of bubbles has generally been circumvented, no such method of removing bubbles that adhere on the 2D material/solution interface has been reported. Here, we report a scalable method at removing micro-bubbles on the surface of CVD graphene by using hydrophobic surfaces modified by self-assembled monolayers (SAMs), which allows the graphene film to flatten before transfer to a substrate, and significantly improves the large-area electrical performance of devices. The enhanced electrical properties are shown to arise from decreased tears and wrinkles produced from trapped bubbles. The bubble removal method can be adapted to wafer-scale processing and will lead to defect-free 2D electrical devices with uniform device performance across large-areas.

During transfer, because it is unfavorable for bubbles to be in contact with water,[15] bubbles generated in solution prefer to adhere to the hydrophobic graphene surface.[16] One means to remove these bubbles is by a "dry transfer" method, where the graphene is completely removed from solution by using exclusively designed rigid supports such as thermal release tape or pressure sensitive polymers.[17–19] Instead, we investigated a simple "wet transfer" method that can be easily implemented using counter-adhesion from a hydrophobic surface. The hydrophobic surface that is used in this work is a vapor deposited SAM of 1H,1H,2H,2H-perfluorodecyltrichlorosilane (FDTS) on a silicon-oxide (SiO_2) layer on silicon (Si). Following SAM functionalization, the surface becomes hydrophobic (see supplementary Fig. 1) and can be used for bubble removal during graphene transfer.

To grow large-domain monolayer graphene on copper foils, we use an oxygen-assisted CVD process with two-stages of methane flow rate to first, decrease the nucleation density, and then, promote edge-growth until a full film forms.[20] Following graphene synthesis, the graphene films can be "wet transferred" following the standard protocol using a poly(methyl methacrylate) (PMMA) support layer. The graphene/PMMA stack is then removed from the copper foil growth substrate using an electro-delamination process in NaOH solution, where the copper/graphene/PMMA is used as the cathode and a carbon rod is used as the anode. Previously, researchers have used a small voltage between the cathode and anode in order to deliberately avoid the generation of bubbles on the graphene surface.[10] Instead, as the main purpose of this work, the generation of bubbles is not avoided (as the bubbles will be removed using the hydrophobic SAM wafer) and the voltage used to delaminate does not need to be delicately tuned. The bubble removal process is illustrated in Fig. 1 and described below.

The process begins after the graphene/PMMA stack is delaminated from the copper foil where bubbles generated on the graphene surface cause rippling [Fig. 1(a)]. The floating graphene/PMMA stack is then moved to a clean deionized (DI) water bath, as per standard transfer process. While in DI water, the graphene/PMMA film is brought into contact with the hydrophobic SAM wafer by "scooping" [Fig. 1(b)]. The bubbles act as a capillary bridge between the substrate and the graphene film,[15] which prevents irreversible adhesion to the wafer that would damage the graphene film.[21] By

[a)]Author to whom correspondence should be addressed: pburke@uci.edu

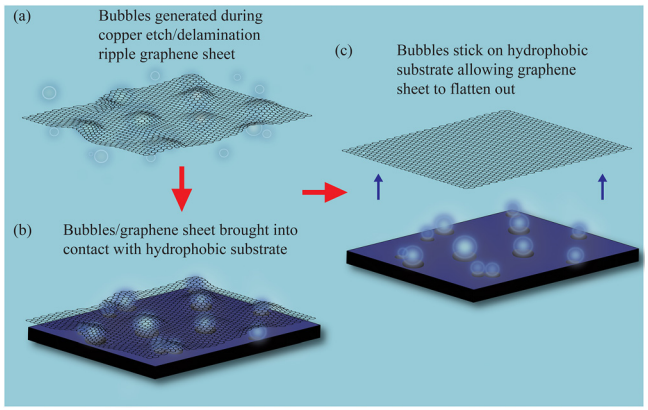

FIG. 1. Illustration of bubble removal process: (a) Bubbles are generated in solution during the etch/delamination step when CVD grown graphene is removed from the growth substrate (copper foil). Bubbles stick to the bottom side (in contact with solution) of the floating graphene film. (b) The graphene film with bubbles on the bottom side is brought into contact with a SAM modified SiO_2 chip. (c) The hydrophobic bubbles adhere to the hydrophobic SAM surface, which removes the bubbles from the graphene surface, and allows the floating graphene film to flatten out.

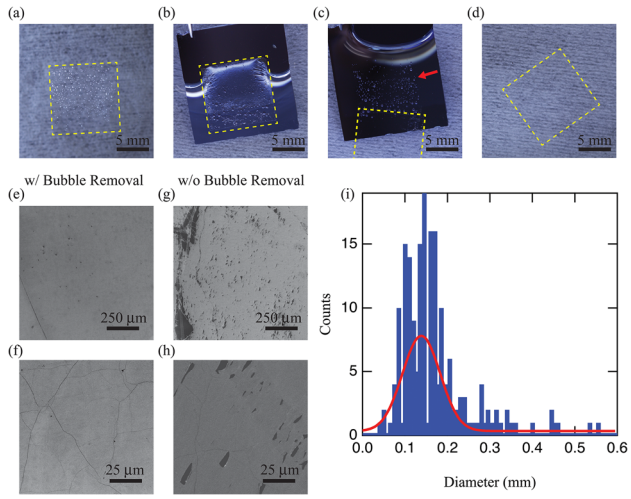

FIG. 2. Removal of bubbles from graphene surface: (a) Floating graphene film (covered with PMMA) contains bubbles on the bottom surface generated during electro-delamination. A yellow dotted line is provided to help identify the boundaries of the floating graphene/PMMA film. (b) The graphene/PMMA stack is brought into contact with the hydrophobic SAM modified SiO_2 chip by "scooping." (c) By submerging the hydrophobic SAM modified wafer beneath water, the graphene/PMMA is released to float on the water surface, while the bubbles remain on the hydrophobic SAM modified chip. A red arrow points to bubbles that remain on the SAM modified chip. (d) A bubble-free graphene film floats on the surface of water and is ready to be transferred to the desired target substrate. (e), (f) SEM images of a graphene film transferred to an oxide-on-silicon chip following bubble removal. (g), (h) SEM images of a graphene film transferred to an oxide-on-silicon chip without bubble removal. Without removing the bubbles from the bottom side of the graphene film, bubbles become trapped between the graphene film and the target substrate, resulting in detrimental tears in the graphene film after drying. (i) Histogram of the diameter of bubbles on the graphene surface generated during electro-delamination. The diameter distribution was analyzed with a Gaussian fit, with a value centered at ~140 μm.

submerging the wafer into DI water, the graphene film is subsequently released from the hydrophobic wafer, though the bubbles stay adhered to the hydrophobic substrate. This allows the bubble-free graphene film to flatten out on the surface of the DI water [Fig. 1(c)].

Figures 2(a)–2(d) contain optical images of bubble removal from an actual graphene film. Figure 2(a) shows a floating graphene/PMMA film with a clear evident of bubbles on the bottom. A yellow dotted line was added to help identify the boundary of the film. In Fig. 2(b), the graphene/PMMA film is "scooped" from DI water using the hydrophobic modified substrate, with half of the film still floating in DI water, while the other half is "pinned" to the substrate. After the film makes full contact with the hydrophobic substrate, the substrate is immersed back into DI water to release the film, allowing the graphene to float to the surface of DI water. Even as the graphene/PMMA film floats away, the square imprint of the bubbles is apparent on the hydrophobic substrate, highlighted by the red arrow in Fig. 2(c). Upon exposing the hydrophobic substrate to air, the bubbles can be simply popped, and hence, the substrate can be readily reused for further bubble removal from the graphene film. Because the amount of bubbles removed can depend on the operational proficiency of the "scooping" method, to improve the efficacy of the method, the bubble removal procedure is repeated thrice on the same film, each time rotating the graphene film by 90°. We found that repeating the bubble removal process thrice was sufficient to fully remove all bubbles from the graphene surface. Figure 2(d) shows the floating graphene/PMMA film with all bubbles removed, ready for transfer to the desired target substrate.

Figures 2(e) and 2(f) comprise of scanning electron microscopy (SEM) images of transferred graphene films (with the PMMA support layer removed) after utilizing the bubble removal process. To compare, Figs. 2(g) and 2(h) show SEM images of transferred graphene films without the bubble removal process. In both cases, wrinkles typical to CVD grown graphene, due the difference of thermal expansion of graphene and the copper grown substrate generated upon cooling[1] are observed. Notably, without the bubble removal process, the SEM images in Figs. 2(g) and 2(h) includes a large number of tears in the graphene film, not present when the bubble removal process is used. These images show that the flattening of the graphene film before transfer prevents the formation of tears produced by trapped bubbles.[12] Furthermore, supplementary Fig. 2 contains optical photographs of transfers with and without bubble removal. Large-scale wrinkles in the graphene film, caused by the trapping of bubbles between the graphene film and the target substrate film (not from the CVD cooling process), are clearly evident in the case where bubbles are not removed.

Using the optical image in Fig. 2(a), we estimate the size of bubbles removed using the image analysis software. The bubble diameter distribution is plotted in Fig. 2(i), and a Gaussian fit yields a diameter centered at ~140 μm, although a tail of large bubbles is present, with ~23% of bubbles >0.20 mm (the 1σ threshold). However, nanoscale tears in Fig. 2(h) suggest that nanoscale bubbles that exist on the graphene surface are removed using the bubble removal process, but we have not confirmed this with nano-imaging. Nonetheless, the removal of micro-scale to mm-scale bubbles effectively decreases micro-scale to mm-scale tears and wrinkles in the graphene film.

In order to investigate the effects of removing micro-scale to mm-scale bubbles on the graphene device performance, we

perform a variety of large-area (mm-scale) characterization. The large-area measurements allow us to probe collective device behavior that, elsewise, could be undetectable at micro-scale dimensions. Following transfer to an oxide on Si wafer (and PMMA removal), we deposit chromium/gold contacts to probe the graphene electrical properties. Figure 3(a) shows the large-area source-drain current versus gate voltage of devices of dimensions $\sim 7 \times 4.5$ mm with and without prior bubble removal. Although the charge neutral point voltage (V_{CNP}) is nearly identical for both cases, removing bubbles from the graphene surface results in increased large-area field-effect mobility compared to when bubbles are not removed, as evident in the depletion curve data. We define the on/off ratio as the ratio of the current at 0 V_g to the current at V_{CNP}; the on/off ratio is $\sim$10 ($2\times$ larger than when bubble removal is not used), consistent with increased mobility (see supplementary Table 1). Using the equation, $\mu_{FE} = \frac{\partial I_{DS}}{\partial V_g} \frac{1}{V_{DS}} \frac{L}{W} \frac{1}{C_{ox}}$, where I_{DS} is the measured source-drain current, V_{DS} is the applied source-drain voltage,

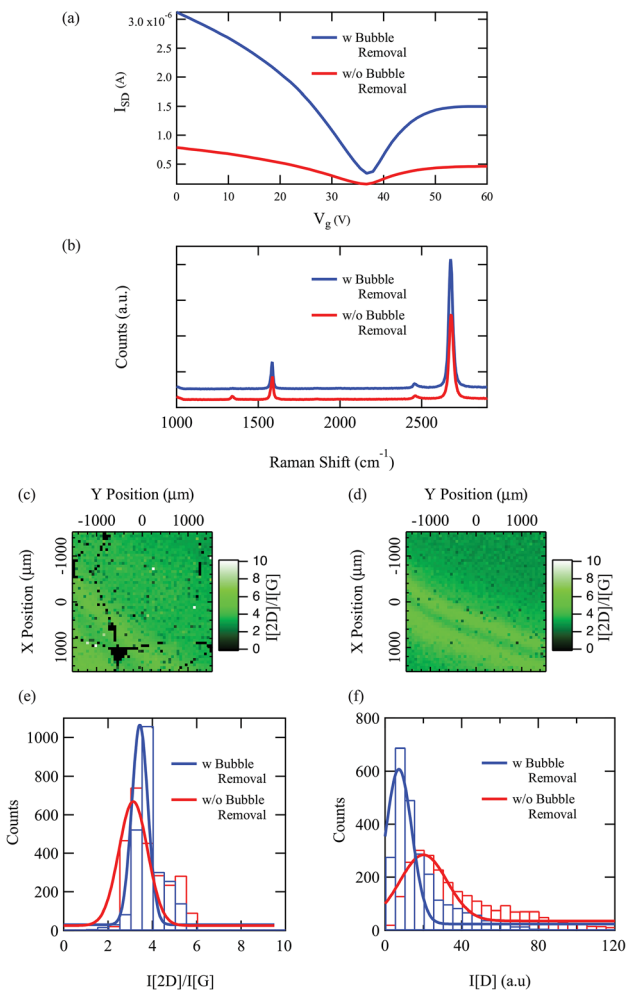

FIG. 3. Large-area characterization of devices with bubble removal: (a) The source-drain current versus gate voltage is measured over large-areas (mm-scale) for devices with and without bubble removal. With bubble removal, the on/off ratio is increased to $\sim$10. (b) Representative Raman spectra of transferred graphene films with and without bubble removal. (c), (d) Raman mapping data of the I[2D]/I[G] for devices fabricated both without and with bubble removal. Cracks and tears in the graphene film from trapped bubbles during transfer are apparent. (e) Histograms of the I[2D]/I[G] for graphene films with and without bubble removal. (f) Histograms of the D peak intensity for graphene films with and without bubble removal.

L is the device length, W is the device width, C_{ox} is the oxide capacitance, and V_g is the gate voltage applied, we calculate the large-area field-effect mobility.[22] The greatest field-effect hole mobility calculated for large-area devices is $\sim$3260 cm^2 V^{-1} s^{-1} (compared to $\sim$868 cm^2 V^{-1} s^{-1} without bubble removal).

We also measured the large-area (zero gate biased) sheet resistance to quantify the effects of removing bubbles before transfer. We used a shadow mask to deposit four contact electrodes separated by 5 mm in a square geometry to ensure that probed area is equivalent for each device. Supplementary Table 1 lists the sheet resistance values for devices with and without bubble removal. For devices with and without bubble removal, the average sheet resistance is $\sim$705 Ω/□ and $\sim$1289 Ω/□, respectively. The lowest sheet resistance values obtained is $\sim$466 Ω/□ when bubbles are removed, and $\sim$1277 Ω/□ when bubbles are not removed prior to device fabrication. The combination of increased large-area mobility and decreased large-area sheet resistance confirms that electrical quality of graphene devices is improved by the bubble removal process.

The improved electrical properties by bubble removal can also be supported using Raman Spectroscopy. The Raman spectra of monolayer graphene exhibits two distinct peaks called the G peak ($\sim$1583 cm^{-1}) and the 2D peak ($\sim$2680 cm^{-1}).[23,24] Another peak called the D peak ($\sim$1350 cm^{-1}) is often used to quantify defects.[23,24] For high quality graphene without defects, the ratio 2D:G peak intensities should be as large as possible (>2 for monolayer graphene), and the D peak intensity should be as low as possible.[23,24] The representative Raman spectra of transferred samples with and without using bubble removal are shown in Fig. 3(b). We performed Raman mapping to assess the graphene quality across large-areas. Presented in Figs. 3(c) and 3(d) are the Raman mapping images of the ratio of the intensities of the 2D:G peaks. The histograms of the 2D:G ratio for samples with and without bubble removal are shown in Fig. 3(e). The histograms reveal the ratio of the 2D:G peak intensities is generally larger (Gaussian fit has larger amplitude, greater in center value, and narrower width) when bubble removal is used, indicating a higher quality graphene than compared to when bubble removal is not used . Also, clearly displayed in Raman mapping image [Fig. 3(c)] (when bubble removal is not utilized) are areas where the 2D:G peak intensity is approximately zero; these areas are undoubtedly where cracks and tears exist, and hence do not exhibit the distinct graphene peaks. The cracks and tears can also affect the spatial variation of the D peak. The histograms of the D peak for samples with and without bubble removal are shown in Fig. 3(f) and confirm that the sample without bubble removal exhibits more frequent and higher intensity D peak, though, as discussed in supplementary Fig. 3; the I[2D]/I[G] data are less susceptible to errors from the laser moving out of focus during Raman mapping. Collectively, the information presented from the Raman mapping experiments confirm that the electrical quality of transferred graphene devices is significantly improved using bubble removal.

Although our studies can be directly utilized in applications that require high-electronic-quality large-area graphene

such as graphene-terahertz devices,[25–27] the developed bubble removal method can also improve large-area 2D insulators such as hexagonal boron nitride (h-BN) by reducing pinholes and decreasing wrinkles. We have also used the FDTS SAMs for bubble removal on the surface of h-BN films supplementary Fig. 4. Hydrophobic functionalization is not limited to the FDTS SAMs used in this work; we have also experimented with octadecyltrichlorosilane (ODTS) SAMs (supplementary Fig. 1) with similar effectiveness in bubble removal, but possible differences in efficacy have not been quantified. Depending on the chosen SAM, it is plausible that the interaction with the graphene (2D material) film may inhibit release from the substrate, and thus, the choice of SAM may need to be tailored for each material of choice in future uses. However, vapor deposited SAM functionalization can be performed on full wafers, and hence, the developed method provides a scalable means for bubble removal from large-area 2D materials.

Another advantage of the developed bubble removal method is that, once the graphene film is released from the hydrophobic substrate, the adhered bubbles can be cleared simply by pulling the wafer out of solution. The electrical data from our devices were compared with both wet transfer (including bubble free methods) and dry transfer (where we assume no surface bubbles exist) in supplementary Table 2 and show that our method improves wet transferred devices to perform comparably to dry transfer devices reported in the literature. Our facile technique allows the process to be quickly cycled, and more importantly, the functionalized wafer is readily available for further bubble removal. The reusability aspect is not true for dry transfer techniques that use of non-reusable materials such as thermal release tape.[17,18] We have used one single functionalized wafer for repeated bubble removal without noticeable degradation over 100 times.

We have developed a scalable and reusable bubble removal method using hydrophobic functionalized surfaces that reduce tears and wrinkles created by trapped bubbles between transferred graphene films and the target substrate to improve the large-area electronic quality of graphene devices. We confirm that the developed bubble removal method results in improved large-area mobility (device on/off ratio), and decreased (zero gate-biased) sheet resistance. Following bubble removal, the high-quality graphene was also confirmed using Raman spectroscopy mapping and shows increased 2D:G peak ratio and decreased the D peak intensity across large areas. Our bubble removal method could find wide use in applications such as large-area 2D optoelectronics and wafer-scale fabrication of 2D heterojunction devices.

A SiO_2 on Si wafer is first cleaned in hot piranha at 120 °C for 1 h. Following piranha clean, the hydrophilic wafer is rinsed with DI water and dried. Then, the wafer is placed in a vacuum chamber with ~50 μl of FDTS solution in a glass vial. The chamber is evacuated, then sealed. After 6 h, the wafer is removed, and hydrophobic functionalization is confirmed by water contact angle.

Large-domain monolayer graphene films are grown on copper foils by low pressure chemical vapor deposition in an evacuated 5-in. quartz tube using a fast, oxygen-assisted growth process following Ref. 20 Briefly, at 1030 °C, two-stages of methane flow (0.8 sccm and 2.4 sccm) are used to control graphene nucleation density and edge growth until individual domains merge to form a full film.

Following CVD growth, graphene films on copper foil are covered with a layer of PMMA and baked. The backside graphene is then removed in O_2 plasma, and the sample is placed in a 60 °C oven overnight. Samples are cut to $\sim 1.5 \times 1.5\,cm^2$ for transfer. The graphene/PMMA stack is delaminated from the copper foil in a 0.2 M NaOH solution using 2.7 V between the graphene sample and a carbon rod. The delamination process generates bubbles that stick to the bottom side of the floating graphene/PMMA stack. Following delamination, the graphene/PMMA stack can be wet transferred to the desired target substrate. In this work, the substrate is 10 nm Al_2O_3 deposited via atomic layer deposition (ALD) on 90 nm SiO_2 on a high resistivity silicon (Si) substrate. The PMMA layer is removed in acetone. H-BN films purchased from graphene-supermarket are transferred using the same protocol.

Four Cr/Au (20/50 nm) electrodes were deposited by electron beam evaporation in a square layout separated by 5 mm width for electrical characterization. Large-area sheet resistance measurements were performed using a 4-point van der Pauw method with a lock-in amplifier. Depletion curve measurements were performed on diagonally opposed contacts as the source-drain electrodes (separated by ~7 mm) with the gate voltage applied to the silicon layer.

SEM images were obtained using a FEI Magellan 400 XHR SEM. Imaging was performed using 1 kV acceleration voltage and 0.1 nA beam current.

Raman spectroscopy was performed using a Renishaw InVia Raman Spectrometer with a 532 nm laser. Raman mapping was performed in a $\sim 3 \times 3$ mm area, with 60 μm step size and 0.7 second acquisition time. Peak fitting was performed using the Renishaw WiRE software. The extracted peak fitting was plotted using Igor Pro 7.

Optical photographs of graphene films with bubbles were imaged using an 18-megapixel Canon EOS 650 D with a 100 mm macrolens. The diameter of the bubbles was estimated using ImageJ software, with the scale calibrated to 1 mm. Gaussian fitting of the diameter size was performed using Igor Pro 7.

See supplementary material for contact angle, large scale wrinkle characterization, Raman focusing procedure, H-BN transfer, and electrical data.

We appreciate the conversations with D. Fishman, J. Hes, and S. Martinez. SEM and oxygen plasma work were performed at the Irvine Materials Research Institute (IMRI). Raman spectroscopy work was performed at the UC Irvine Laser Spectroscopy Facility (LSF). CVD synthesis and e-beam evaporation were performed at the Integrated Nanosystems Research Facility (INRF).

This work was funded by the Army Research Office through the ARO-MURI Program, ARO-Core Grants, and DURIP (Contract Nos.: W911NF-11-1-0024, W911NF-18-1-0076, W911NF-09-1- 0319, and W911NF-11-1-0315), and National Institutes of Health (Contract Nos.: CA182384).

The authors declare no competing financial interest.

[1]X. Li, W. Cai, J. An, S. Kim, J. Nah, D. Yang, R. Piner, A. Velamakanni, I. Jung, E. Tutuc, S. K. Banerjee, L. Colombo, and R. S. Ruoff, Science **324**, 1312 (2009).
[2]C. Mattevi, H. Kim, and M. Chhowalla, J. Mater. Chem. **21**, 3324 (2011).
[3]T. Liang, C. Luan, H. Chen, and M. Xu, Nanoscale **9**, 3719 (2017).
[4]K. K. Liu, W. Zhang, Y. H. Lee, Y. C. Lin, M. T. Chang, C. Y. Su, C. S. Chang, H. Li, Y. Shi, H. Zhang, C. S. Lai, and L. J. Li, Nano Lett. **12**, 1538 (2012).
[5]Y. Zhan, Z. Liu, S. Najmaei, P. M. Ajayan, and J. Lou, Small **8**, 966 (2012).
[6]L. Song, L. Ci, H. Lu, P. B. Sorokin, C. Jin, J. Ni, A. G. Kvashnin, D. G. Kvashnin, J. Lou, B. I. Yakobson, and P. M. Ajayan, Nano Lett. **10**, 3209 (2010).
[7]Y. Chen, X. L. Gong, and J. G. Gai, Adv. Sci. **3**, 8 (2016).
[8]M. Chen, R. C. Haddon, R. Yan, and E. Bekyarova, Mater. Horiz. **4**, 1054 (2017).
[9]J. W. Suk, A. Kitt, C. W. Magnuson, Y. Hao, S. Ahmed, J. An, A. K. Swan, B. B. Goldberg, and R. S. Ruoff, ACS Nano **5**, 6916 (2011).
[10]C. T. Cherian, F. Giustiniano, I. Martin-Fernandez, H. Andersen, J. Balakrishnan, and B. Özyilmaz, Small **11**, 189 (2015).
[11]Y. Wang, Y. Zheng, X. Xu, E. Dubuisson, Q. Bao, J. Lu, and K. P. Loh, ACS Nano **5**, 9927 (2011).
[12]T. Hallam, N. C. Berner, C. Yim, and G. S. Duesberg, Adv. Mater. Interfaces **1**, 1400115 (2014).
[13]X. Liang, B. A. Sperling, I. Calizo, G. Cheng, C. A. Hacker, Q. Zhang, Y. Obeng, K. Yan, H. Peng, Q. Li, X. Zhu, H. Yuan, A. R. H. Walker, Z. Liu, L. M. Peng, and C. A. Richter, ACS Nano **5**, 9144 (2011).
[14]F. Pizzocchero, B. S. Jessen, P. R. Whelan, N. Kostesha, S. Lee, J. D. Buron, I. Petrushina, M. B. Larsen, P. Greenwood, W. J. Cha, K. Teo, P. U. Jepsen, J. Hone, P. Bøggild, and T. J. Booth, Carbon **85**, 397 (2015).
[15]P. Attard, Langmuir **12**, 1693 (1996).
[16]J. Rafiee, X. Mi, H. Gullapalli, A. V. A. V. A. Thomas, F. Yavari, Y. Shi, P. M. Ajayan, and N. A. Koratkar, Nat. Mater. **11**, 217 (2012).
[17]S. Bae, H. Kim, Y. Lee, X. Xu, J. S. Park, Y. Zheng, J. Balakrishnan, T. Lei, H. Ri Kim, Y. Il Song, Y. J. Kim, K. S. Kim, B. Özyilmaz, J. H. Ahn, B. H. Hong, and S. Iijima, Nat. Nanotechnol. **5**, 574 (2010).
[18]J. Kang, S. Hwang, J. H. Kim, M. H. Kim, J. Ryu, S. J. Seo, B. H. Hong, M. K. Kim, and J. B. Choi, ACS Nano **6**, 5360 (2012).
[19]S. J. Kim, T. Choi, B. Lee, S. Lee, K. Choi, J. B. Park, J. M. Yoo, Y. S. Choi, J. Ryu, P. Kim, J. Hone, and B. H. Hong, Nano Lett. **15**, 3236 (2015).
[20]P. H. Q. Pham, W. Zhou, N. V. Quach, J. Li, J.-G. Zheng, and P. J. Burke, Chem. Mater. **28**, 6511 (2016).
[21]L. Gao, G.-X. Ni, Y. Liu, B. Liu, A. H. C. Neto, and K. P. Loh, Nature **505**, 190 (2014).
[22]F. Schwierz, Nat. Nanotechnol. **5**, 487 (2010).
[23]A. C. Ferrari, J. C. Meyer, V. Scardaci, C. Casiraghi, M. Lazzeri, F. Mauri, S. Piscanec, D. Jiang, K. S. Novoselov, S. Roth, and A. K. Geim, Phys. Rev. Lett. **97**, 187401 (2006).
[24]A. Das, S. Pisana, B. Chakraborty, S. Piscanec, S. K. Saha, U. V. Waghmare, K. S. Novoselov, H. R. Krishnamurthy, A. K. Geim, A. C. Ferrari, and A. K. Sood, Nat. Nanotechnol. **3**, 210 (2008).
[25]B. Sensale-Rodriguez, R. Yan, M. M. Kelly, T. Fang, K. Tahy, W. S. Hwang, D. Jena, L. Liu, and H. G. Xing, Nat. Commun. **3**, 780 (2012).
[26]J. D. Buron, F. Pizzocchero, P. U. Jepsen, D. H. Petersen, J. M. Caridad, B. S. Jessen, T. J. Booth, and P. Bøggild, Sci. Rep. **5**, 12305 (2015).
[27]P. H. Q. Pham, W. Zhang, N. V. Quach, J. Li, W. Zhou, D. Scarmardo, E. R. Brown, and P. J. Burke, Nat. Commun. **8**, 2233 (2017).

Supplementary Information

Scalable and Reusable Micro-Bubble Removal Method to Flatten Large-Area 2D Materials

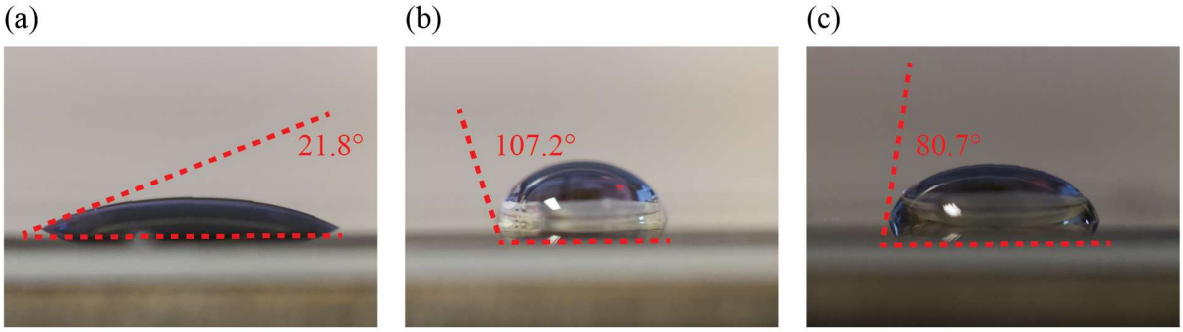

Supplementary Figure 1: a) Contact angle measurement for unmodified SiO_2 on Si wafer. b) Contact angle measurement for 1H,1H,2H,2H-perfluorodecyltrichlorosilane (FDTS) self-assembled monolayer modified SiO_2 on Si wafer. c) Contact angle measurement for octadecyltrichlorosilane (ODTS) self-assembled monolayer modified SiO_2 on Si wafer

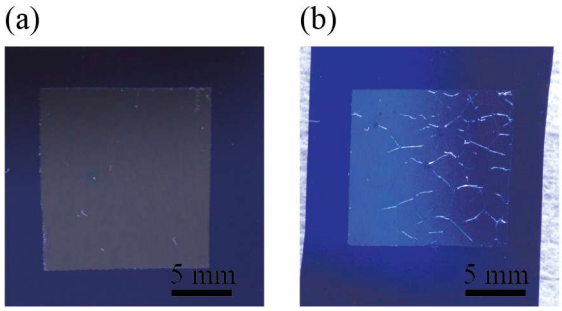

Supplementary Figure 2: Graphene with PMMA film transferred onto target substrate with bubble removal processs. b) Graphene with PMMA film transferred onto target substrate without bubble removal process. Trapped bubbles between graphene and the target substrate cause large wrinkles and tears in the transferred film after drying.

Before performing the mapping function for each device, the Raman spetrometer is focused at the center location (x = 0, y = 0). Supplementary Figure 3 shows the measured Raman spectra of two devices at the center location. Here, the measured intensities of the G and 2D peak for both devices are approximate equal in counts. The mapping function maps 2600 data points starting from the x = -1500, y = -1500 location, rastering the computer controlled stage to the x = 1500, y = 1500 location. Because the mapping measurement is performed across a large area (3x3 mm^2) the laser spot moves slightly out of focus during the measurement. Although this would affect the measured intensities of the individual peaks, since the G and 2D peak will both decrease in intensity as the laser moves out of focus, by taking the ratio of the peaks (G and 2D), the spatial variation in peak intensity is mitigated when assessing graphene quality. Hence, comparing the I[2D]/I[G] from sample to sample is a better gaug of graphene quality than just assessing the D peak.

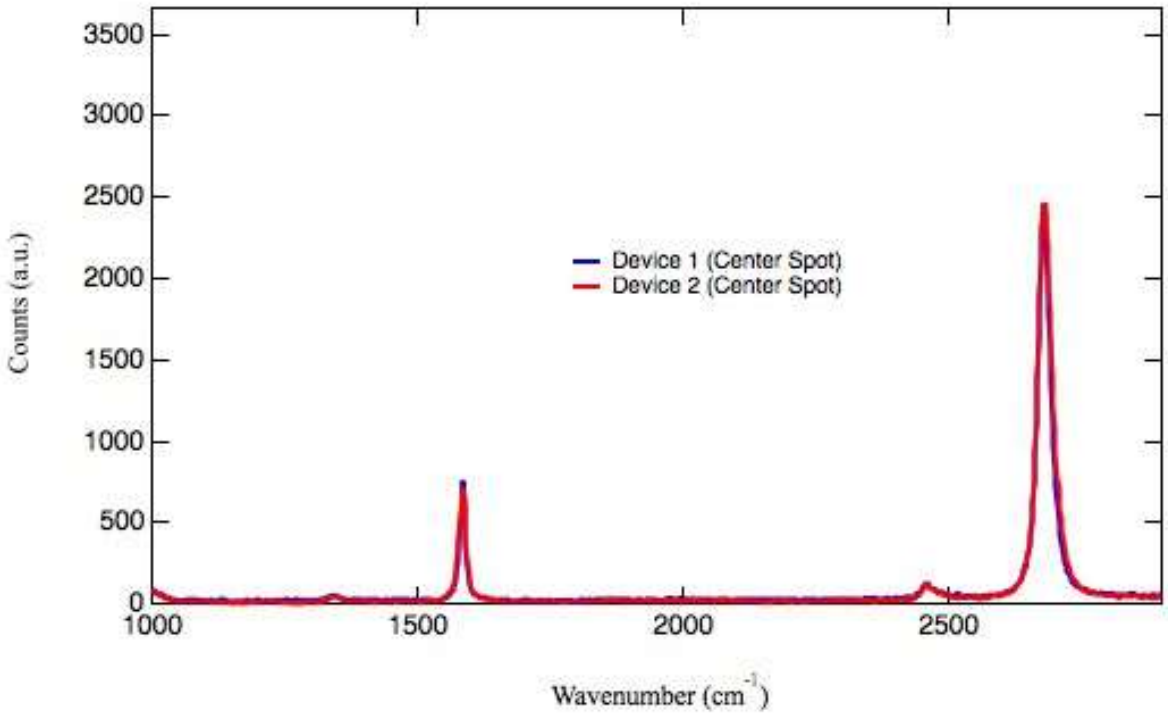

Supplementary Figure 3: Raman spectra of two devices (with and without bubble removal) measured at the center location (x = 0, y = 0).

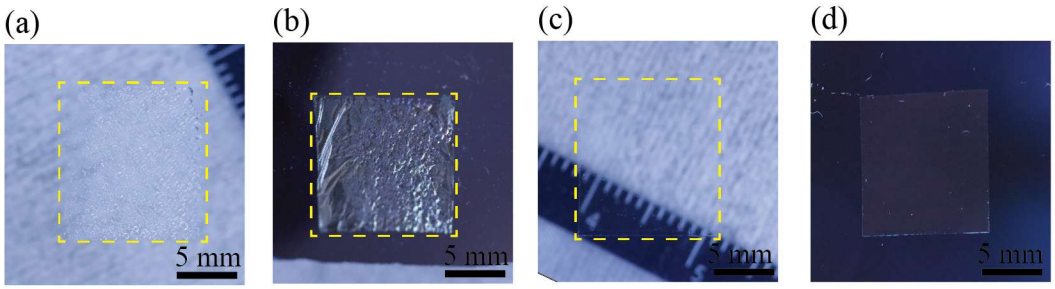

Supplementary Figure 4: Bubble removal process using FDTS hydrophobic substrate to remove bubbles from multilayer hexagonal boron nitride (HBN) film purchased from graphene-supermarket. a) Bubbles generated from the electro-delamination process adhere to the bottom surface of the HBN/PMMA film. b) Bubbles removed by contacting with the FDTS SAM modified substrate. c) Floating HBN/PMMA film without bubbles on the bottom surface. d) Transferred HBN/PMMA film on target substrate following bubble removal and drying. Bubble removal also works for HBN (not limited to just graphene films) and results in flat large-area films without tears and wrinkles.

Device Number	With or Without Bubble Removal	Sheet Resistance (Ω/□)	Field-effect Mobility (cm^2/Vs)	On/Off Ratio
1	With	1525	1.09E+03	5.11
2	With	770	8.41E+02	4.69
3	With	702	1.56E+03	3.81
4	With	844	1.82E+03	7.07
5	With	498	3.18E+03	8.37
6	With	521	3.15E+03	9.19
7	With	489	3.26E+03	10.3
8	With	541	2.71E+03	9.71
9	With	697	2.87E+03	8.3
10	With	466	2.88E+03	10.2
11	Without	1277	8.58E+02	4.86
12	Without	1305	7.15E+02	5.1
13	Without	1285	8.68E+02	6.15

Supplementary Table 1: Electrical characterization of devices with and without bubble removal. The device sheet resistance, estimated field effect hole mobility, and on/off ratio are listed.

Reference Number in Main Text	Transfer Method	Sheet Resistance	Mobility
[9]	Wet Transfer	980 Ω/□	-
[10]	Bubble-Free Wet Transfer	773 Ω/□	-
[12]	Wet Transfer	-	1600 cm^2/Vs
[13]	Wet Transfer	-	1400 cm^2/Vs
[14]	Bubble-Free Wet Transfer	1111 Ω/□	1930 cm^2/Vs
[17]	Roll-to-Roll Dry Transfer	275 Ω/□	5100 cm^2/Vs
[18]	Hot Pressing Dry Transfer	397 Ω/□	-
[19]	Pressure Sensitive Polymer Dry Transfer	250 Ω/□	5300 cm^2/Vs

Supplementary Table 2: The electrical data from the transfer techniques referenced in the main manuscript are compared.